Journal of
Nanoscience and Nanotechnology
Vol. 13, 4962–4968, 2013

Supported F-Doped α-Fe_2O_3 Nanomaterials: Synthesis, Characterization and Photo-Assisted H_2 Production

Giorgio Carraro[1], Davide Barreca[2], Daniela Bekermann[1], Tiziano Montini[3], Alberto Gasparotto[1], Valentina Gombac[3], Chiara Maccato[1,*], and Paolo Fornasiero[3]

[1] Department of Chemistry, Padova University and INSTM, 35131 Padova, Italy
[2] CNR-ISTM and INSTM, Department of Chemistry, Padova University, 35131 Padova, Italy
[3] Department of Chemical and Pharmaceutical Sciences, Trieste University, INSTM and ICCOM-CNR Trieste Research Unit, 34127 Trieste, Italy

Supported fluorine-doped α-Fe_2O_3 nanomaterials were synthesized by Plasma Enhanced-Chemical Vapor Deposition (PE-CVD) at temperatures between 300 and 500 °C, using a fluorinated iron(II) diketonate-diamine compound as a single-source precursor for both Fe and F. The system structure, morphology and composition were thoroughly investigated by various characterization techniques, highlighting the possibility of controlling the fluorine doping level by varying the sole growth temperature. Photocatalytic H_2 production from water/ethanol solutions under simulated solar irradiation evidenced promising gas evolution rates, candidating the present PE-CVD approach as a valuable strategy to fabricate highly active supported materials.

Keywords: Iron Oxide, Fluorine Doping, Plasma Enhanced-Chemical Vapor Deposition, Solar Hydrogen Production, Photoreforming.

RESEARCH ARTICLE

1. INTRODUCTION

Photo-assisted hydrogen generation from aqueous solutions is a key scientific and technological challenge to convert solar radiation into fuels, meeting the actual demand of clean and renewable energy sources.[1–9] In this regard, the development of metal oxide photocatalysts, especially if supported on suitable substrates, has attracted a considerable attention for direct *on-site* technological utilizations.[4,7] Among the possible active materials, iron(III) oxides display various inherent advantages, such as abundance, low cost, non-toxicity and rich family of polymorphs with diverse functional properties.[1,10,11] In particular, α-Fe_2O_3 (*hematite*, $E_G \approx 2.2$ eV), the most stable Fe_2O_3 phase, has been the subject of intensive studies for solar water splitting, thanks to its low band gap, high activity, facile synthesis and long-term stability.[3,5–7,10,12–15] Nevertheless, key issues to be addressed for an efficient photo-activated H_2 evolution from α-Fe_2O_3 concern the high resistivity, fast recombination of photogenerated electrons/holes (e^-/h^+), and very short charge carrier diffusion length.[1,3,15] In addition, the *hematite* indirect band gap results in a high radiation penetration depth, responsible for a low e^-/h^+ concentration at the material surface.[5] An attractive strategy to overcome the above drawbacks is offered by the chemical modification of α-Fe_2O_3 with suitable doping agents and by the control of the system nano-organization.[4,6–8,14,15] In this context, anion doping of oxide phases, in particular by fluorine, offers several benefits, from an enhanced solar light absorption up to the passivation of surface defects, increasing the lifetime of photogenerated charge carriers.[2,8,9,16,17] Moreover, the electron withdrawing effect exerted by fluorine can increase the chemical reactivity of metal centers, promoting catalytic processes involved in H_2 production.[2,18–22] Yet, in spite of these advantageous effects, F-doping of iron oxide photocatalysts has never been reported in the literature up to date.

In this paper, we present an original PE-CVD approach to supported F-doped iron(III) oxide (F:α-Fe_2O_3) nanomaterials, using a *single-source* precursor $Fe(hfa)_2 \cdot TMEDA$ (hfa = 1,1,1,5,5,5-hexafluoro-2,4-pentanedionate; TMEDA = *N*,*N*,*N*′,*N*′-tetramethylethylenediamine) in Ar/O_2 plasmas.[23,24] Beside the inherent advantages of the

*Author to whom correspondence should be addressed.

1533-4880/2013/13/4962/007 doi:10.1166/jnn.2013.7584

PE-CVD technique, leading to a unique material nano-organization,[25] the formation of fluorinated radicals in the used plasmas enabled an *in-situ* anion doping during the growth process.[2] As a consequence, F:α-Fe_2O_3 nanostructures could be deposited without the need of additional toxic/corrosive fluorinating reactants (such as CF_4, F_2, NH_4F). PE-CVD of iron oxide was performed between 300 and 500 °C and followed by a multi-technique characterization, with particular attention on the system structure, morphology and composition. The obtained results highlighted the possibility of growing F-doped iron(III) oxide nanomaterials, with a fluorine content tunable as a function of the growth temperature. The synthesized systems were also tested in H_2 production by photoreforming[26] from water/ethanol solutions under simulated solar irradiation, yielding photocatalytic performances dependent on the F:α-Fe_2O_3 synthetic parameters and fluorine content.

2. EXPERIMENTAL DETAILS

2.1. Synthesis

The $Fe(hfa)_2 \cdot TMEDA$ precursor was synthesized according to a recently reported procedure.[23, 24] PE-CVD experiments were performed by a two-electrode custom-built PE-CVD apparatus[27] powered by a Radio Frequency (RF, $\nu = 13.56$ MHz) generator. Prior to each growth experiment, Si(100) substrates (1.5×1.5 cm^2, MEMC, Merano, Italy) were cleaned by iterative dipping in sulfonic detergent, distilled water, acetone, and isopropylic alcohol. Electronic grade argon and oxygen were used as plasma sources and introduced into the reactor chamber after pre-evacuation down to 10^{-6} mbar. The precursor, placed in an external vessel heated at 65 °C by an oil bath, was transported toward the deposition zone by an Ar flow (rate = 60 sccm). To prevent undesired condensation phenomena, the gas line temperature was maintained at 140 °C by means of heating tapes. Additional Ar and O_2 flows (rates = 15 and 20 sccm, respectively) were directly introduced into the reactor by two auxiliary gas-lines. For all depositions the total pressure, deposition time, RF-power and interelectrode distance were kept constant at 1.0 mbar, 60 min, 10 W and 6 cm, respectively. The deposition temperature was varied between 300 and 500 °C. The obtained samples were characterized *as-grown* without any further *ex-situ* treatment.

2.2. Characterization

Glancing Incidence X-ray Diffraction (GIXRD) patterns were collected at a constant incidence angle of 1.0° by a Bruker D8 Advance diffractometer equipped with a Göbel mirror, using a CuKα X-ray source powered at 40 kV and 40 mA.

Fourier Transform-Infrared (FT-IR) spectra were collected with a Nexus 870 FT-IR apparatus in the range 350–4000 cm^{-1}, subtracting the Si(100) substrate contribution.

Atomic Force Microscopy (AFM) analyses were performed using a NT-MDT SPM Solver P47H-PRO instrument operating in tapping mode in air. Root-Mean-Square (RMS) roughness values were obtained from 2×2 μm^2 images after a plane fitting procedure. Micrographs were collected in different sample regions in order to check the surface homogeneity.

Field Emission-Scanning Electron Microscopy (FE-SEM) cross-sectional micrographs were collected at a primary beam voltage of 10 kV by means of a Zeiss SUPRA 40VP instrument.

A Perkin Elmer Φ 5600ci spectrometer with an AlKα ($h\nu = 1486.6$ eV) standard source was used for X-ray Photoelectron Spectroscopy (XPS) analyses, at a working pressure lower than 2×10^{-9} mbar. The reported Binding Energies (BEs, uncertainty = $\pm$ 0.2 eV) were corrected for charging by assigning to the C1s line of adventitious carbon a BE of 284.8 eV.[28] The atomic percentages (at.%) were calculated using standard PHI V5.4A sensitivity factors. Peak fitting was performed by means of a least-squares procedure, adopting Gaussian-Lorentzian peak shapes. Ar^+ sputtering was carried out at 3.0 kV, with an argon partial pressure of 5×10^{-8} mbar and a current density of 0.4 mA $\times$ cm^{-2}.

Photoreforming experiments for hydrogen production were carried out on 1:1 H_2O/CH_3CH_2OH mixtures (total volume = 80 mL) in a stainless steel discontinuous batch reactor maintained at 25 °C. Electronic grade Ar (rate = 15 mL $\times$ min^{-1}) was used to collect and transfer gaseous products to the analysis system. Illumination was performed using a Solar Simulator (LOT-Oriel) equipped with a Xe lamp (power = 150 W) and a standard AM 1.5G filter to simulate solar irradiation. The total incident solar irradiance, measured by radiometers in the UV and Visible ranges, was 205 mW $\times$ cm^{-2}. Photocatalytic tests were repeated three times on each sample to check data reproducibility. The estimated uncertainty on each value was estimated to be 5%. For comparison purposes, hydrogen production rates were normalized with respect to the catalyst amount. The latter was estimated by considering the Fe_2O_3 bulk density (5.04 g $\times$ cm^{-3}) as well as the average sample thickness (see Table I) and geometrical area (1.5×1.5 cm^2, see above).

On-line detection of evolved gases was carried out by means of an Agilent 7890A Gas Chromatographer (GC) system, equipped with a 10 way-two loop injection valve. A 5 Å molecular sieve column connected to a Thermal Conductivity Detector (TCD) was used for H_2 quantification. Following previous literature studies, Solar-to-Fuel Efficiency (SFE) values were calculated as:[29, 30]

$$\mathrm{SFE} = \frac{\Phi_{H_2} \times \Delta H^0_{298\ K}}{S} \times 100 \quad (1)$$

Table I. Deposit thickness (evaluated by FE-SEM analyses) and fluorine content for F:α-Fe_2O_3 specimens as a function of the growth temperature.

Growth temperature [°C]	Deposit thickness [nm]	Surface at.% F		
		F^a_{TOT}	F(I)[b]	F(II)[c]
300	350	9.2	3.2	6.0
400	250	3.7	1.9	1.8
500	200	2.4	1.3	1.1

Notes: [a]Total fluorine amount; [b]Lattice fluorine; [c]Fluorine in CF_x groups.

where Φ_{H_2} is the H_2 flow produced by each sample (expressed in mol $\times$ s^{-1} $\times$ cm^{-2}), $\Delta H^0_{298\ K}$ is the combustion enthalpy of H_2 at 298 K (285.8 kJ $\times$ mol^{-1}) and S is the total incident solar irradiance (expressed in W $\times$ cm^{-2}). The product $\Phi_{H_2} \times \Delta H^0_{298\ K}$ represents the energy stored in the produced hydrogen.[30]

3. RESULTS AND DISCUSSION

In this work, three different growth temperatures were adopted for the preparation of iron oxide systems via PE-CVD. Relevant material features are summarized in Table I. As can be observed, a progressive decrease of the overall deposit thickness occurred upon increasing the temperature, a phenomenon ascribed to a less efficient precursor adsorption on the growth surface on going from 300 to 500 °C. The system structure was investigated by means of GIXRD (Fig. 1). As a whole, patterns were characterized by the peaks at $2\vartheta = 24.1°$, $33.1°$, $35.6°$ attributed to the (012), (104), (110) reflections of the α-Fe_2O_3 (*hematite*, hexagonal) phase,[31] while no signals

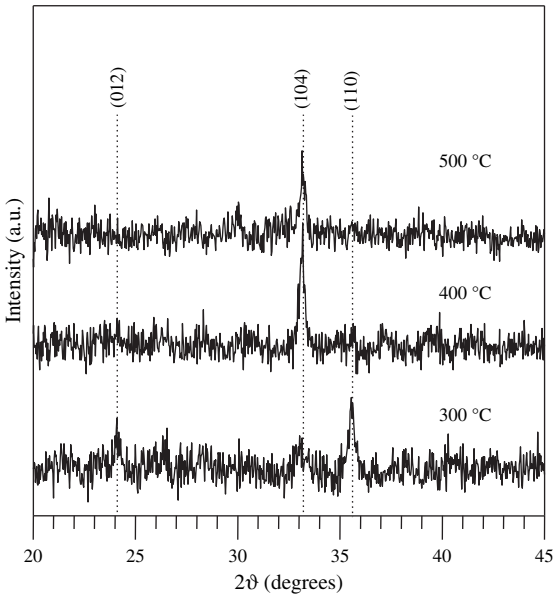

Fig. 1. GIXRD patterns of specimens deposited at 300, 400 and 500 °C. The spectra have been vertically shifted for clarity. Vertical dotted lines mark the reference peak positions for α-Fe_2O_3.[31]

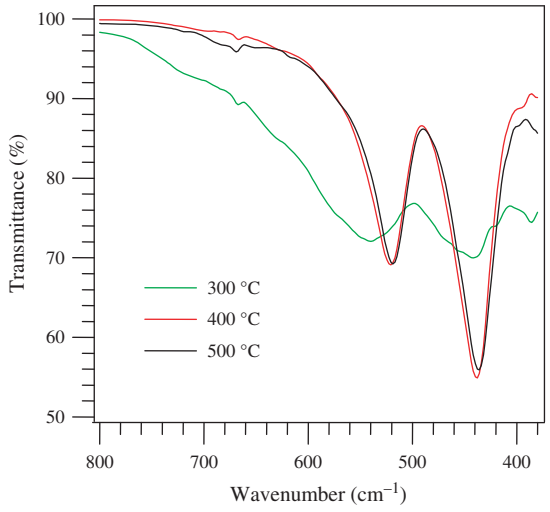

Fig. 2. FT-IR spectra of samples deposited at 300, 400 and 500 °C.

of other iron(III) oxide polymorphs were detected. Interestingly, the growth temperature directly affected the system structure. In fact, a comparison of the recorded intensity ratios with the ones of the reference powder material.[31] evidenced a preferential ⟨110⟩ orientation at 300 °C. On the other hand, at higher growth temperatures, the (104) reflection was the most intense one, as expected for randomly oriented polycrystalline *hematite*.[31] As a general observation, fluorine doping (see below and Table I) did not induce any appreciable shift in the α-Fe_2O_3 reflections, due to the very similar ionic radii of F and O.[17, 32] The mean crystallite size calculated by the Scherrer equation was 30 nm.

In line with GIXRD results, FT-IR measurements (Fig. 2) further confirmed the presence of α-Fe_2O_3. In fact, for specimens grown at 400 and 500 °C, two well-defined absorption bands centred at 440 and 520 cm^{-1} were observed and ascribed to the E_u and A_{2u} *hematite* vibrational modes, respectively.[11, 33] In a different way, the sample deposited at 300 °C showed a peak broadening and slight signal blue-shifts with respect to the other ones. These effects can be traced back to a decreased structural order at lower deposition temperatures, which, in turn, could be related to a higher overall F content (see below and Table I).[33, 34]

The system morphology was analyzed by AFM (Fig. 3). The specimen grown at 300 °C presented an homogeneous distribution of columnar aggregates, while the samples deposited at higher temperatures showed smaller and more interconnected particles. The deposit RMS surface roughness ranged from 15.5 (300 °C) to 5.5 nm (500 °C). As a matter of fact, the system roughness is affected by various parameters, among which surface diffusion (enhanced by high growth temperatures), and plasmochemical etching phenomena (more effective at low temperatures) are likely the most important.

The system chemical composition was analyzed in detail by XPS. Figure 4(a) displays a representative surface

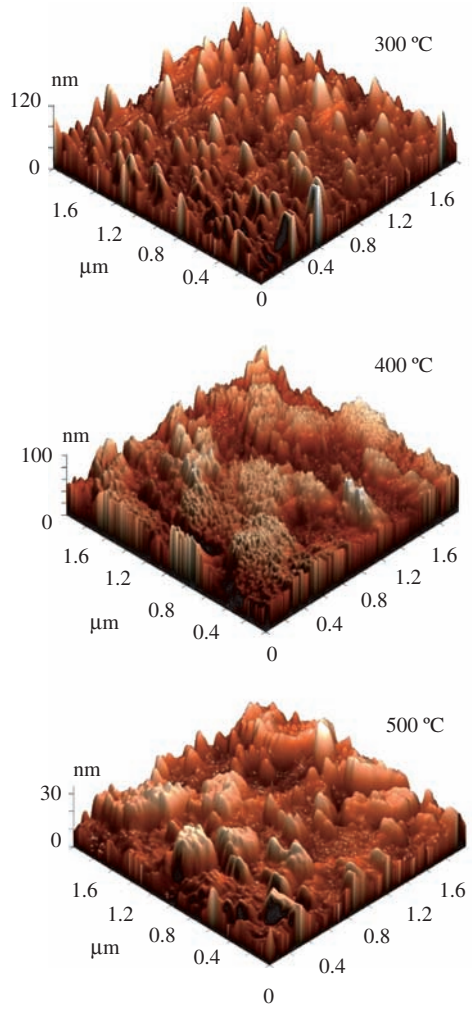

Fig. 3. 2×2 μm^2 AFM micrographs of samples deposited at 300, 400 and 500 °C.

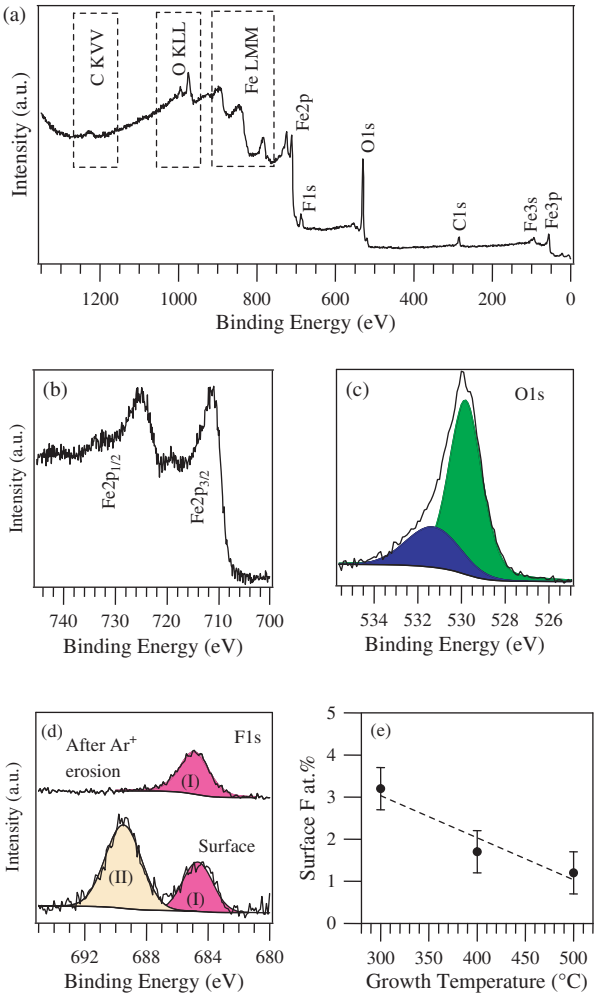

Fig. 4. XPS spectra for an iron oxide specimen grown at 300 °C: (a) survey; (b) Fe2p; (c) O1s; (d) F1s, before and after 20 min Ar^+ erosion; (e) dependence of lattice F surface content on the growth temperature.

wide-scan spectrum, characterized by the predominance of Fe and O photopeaks, along with weaker signals due to C and F species. Carbon concentration was typically 20 at.%. For all the analyzed specimens, the Fe2p peak position [Fig. 4(b); BE($Fe2p_{3/2}$) = 711.3 eV; spin-orbit splitting = 13.8 eV] and shape (low *shake-up* satellites) were in good agreement with literature data for α-Fe_2O_3.[6, 12, 14, 15, 35] The O1s surface photoelectron peak (Fig. 4(c)) was decomposed by means of two contributing bands at BE = 529.9 eV, attributed to lattice oxygen, and 531.4 eV, related to hydroxyl/carbonate species arising from air exposure.[35] As evidenced by Figure 4(d), the surface F1s signal was fitted by means of two different components, located at 684.7 (**I**) and 689.5 (**II**) eV, respectively. Basing on literature data, component (**I**) could be attributed to lattice fluorine in the oxide network, due to the incorporation of F species substitutional to O sites, ruling out fluorine presence at iron oxide grain boundaries in an appreciable amounts.[16, 21, 22] Conversely, the high BE component (**II**) could be ascribed to CF_x moieties from precursor residuals.[2, 21, 36] This component was reduced to noise level after 20 min of Ar^+ erosion (Fig. 4(d)). The concomitant disappearance of the carbon signal upon sputtering demonstrates a clean precursor decomposition under the adopted PE-CVD conditions and highlights the correlation between the presence of carbon species and the fluorine (**II**) component.

Table I reports the overall surface F content, along with the corresponding atomic percentages calculated, by peak fitting, for (**I**) and (**II**) contributions. As can be observed, the growth temperature had a significant influence on the F content. In fact, the maximum overall fluorine percentage was obtained at the lowest growth temperature (300 °C), as already reported for F-doped silicon and cobalt oxides synthetized by PE-CVD.[36, 37] A detailed analysis of the F1s signal revealed that a growth temperature increase resulted not only in a diminished overall F amount, but also in a different relative contribution of (**I**) and (**II**) components (Table I and Fig. 4(e)). This phenomenon indicates that, in spite of the advantages of $Fe(hfa)_2 \cdot TMEDA$ as single-source precursor for F-doped Fe_2O_3, a main issue to

RESEARCH ARTICLE

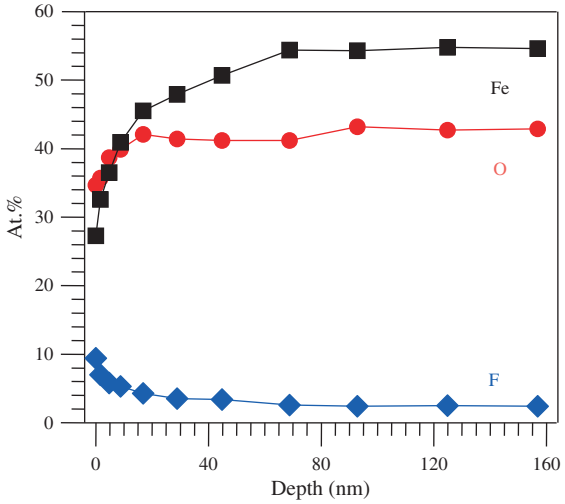

Fig. 5. XPS depth profile for sample obtained at 300 °C.

be properly addressed remains the independent optimization of lattice fluorine and CF_x species content.

Information on the in-depth system composition was obtained by Ar^+ sputtering (Fig. 5). After the first erosion cycles, the average O/Fe atomic ratio became almost constant and displayed a value (≈ 0.8) lower than the stoichiometric one expected for Fe_2O_3, due to oxygen preferential sputtering, as often reported for metal oxides.[28] Concerning fluorine, the initial at.% decrease was mainly attributed to the removal of CF_x contamination (see above), whereas a constant fluorine content (average value ≈ 3 at.%) was present in the inner system region. Such a result indicated a homogeneous fluorine incorporation into the oxide lattice, and supported the successful obtainment of F:α-Fe_2O_3.

Photoreforming experiments on water/ethanol solutions did not yield any appreciable H_2 evolution when illumination and photocatalyst were not simultaneously present. The mechanism for hydrogen evolution by photoreforming of alcohols over metal oxide semiconductors involves H^+ release from the sacrificial agent and the formation of different oxygenated radicals, which are powerful oxidizing agents. The oxidation of adsorbed alkoxide moieties results in the formation of protons, that can decrease the local pH and subsequently be reduced by electron transfer from the semiconductor conduction band. The result is the reduction of protons to H_2 and the concomitant oxidation of the organic compound through various intermediates, including aldehydes and carboxylates, eventually accompanied by dehydration and water gas shift reactions (see Scheme 1).[8, 26]

The H_2 photo-production results under simulated solar irradiation are displayed in Figure 6 for the different specimens. Irrespective of the used growth temperature, all samples presented an initial induction period (≈ 3 h) characterized by a progressive increase of the hydrogen evolution rate. This phenomenon suggested the occurrence of a light-induced surface activation, and the subsequent

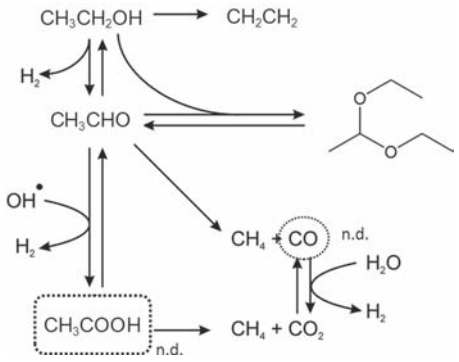

Scheme 1. Possible reaction mechanism involved in the photocatalytic H_2 production over F:α-Fe_2O_3 from aqueous ethanol solutions (n.d. = not detected).

establishment of an equilibrium between the by-products adsorbed on the catalyst surface and in the liquid/gas phase.[2] The use of simulated solar light enabled to perform photocatalytic experiments up to 20 h of irradiation with a nearly constant hydrogen evolution. This issue, highlighting the sample operational stability, discloses attractive perspectives in view of eventual technological applications.

Remarkably, the maximum hydrogen yield, obtained for F:α-Fe_2O_3 deposited at 500 °C (corresponding to 5000 μmol $\times$ h^{-1} $\times$ g^{-1}, SFE = 0.02%) was among the best ever reported for metal oxide systems under similar experimental conditions, also taking into account that no cocatalysts (e.g., Rh, Pd, Pt) were used in this work.[2, 8]

The above results indicate that the present preparative strategy is an amenable route for the production of F:α-Fe_2O_3 photocatalysts joining a remarkable reactivity and an appreciable operational stability. According to previous investigation, the observed variations in the system performances as a function of the growth temperature are not likely related to different band gap values, since

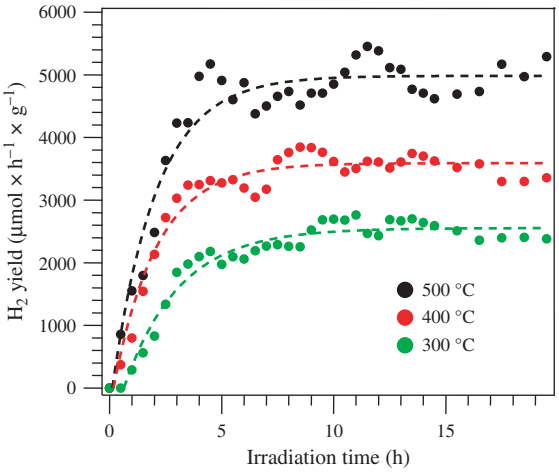

Fig. 6. Hydrogen evolution yields from 1:1 water/ethanol solutions under simulated solar illumination for F:α-Fe_2O_3 specimens deposited at 300, 400 and 500 °C.

F doping has not been reported to appreciably affect this parameter.[2, 21, 38] Additionally, significant contributions from the system surface roughness (a higher roughness likely corresponding to a higher active area) can be ruled out, since, as reported above (see also Fig. 3), the obtained RMS roughness values showed an opposite trend with respect to that of Figure 6. An inspection of Table I reveals that the system functional performances could be directly related to the fluorine percentage, and, in particular, to the beneficial role exerted by lattice fluorine (component (**I**) in Fig. 4(d)). In fact, hydrogen production rate underwent a progressive enhancement upon increasing the growth temperature from 300 to 500 °C. As can be observed, the sample synthesized at 300 °C was characterized by a more than doubled lattice fluorine content with respect to the 500 °C one but, at the same time, by a nearly six-fold higher concentration of CF_x species. It is reasonable to suppose that the latter moieties, being present mainly at the system surface (see the above discussed XPS data), can exert a poisoning effect on the catalyst, with a consequent activity degradation and a detrimental decrease of photoproduced hydrogen yield. This phenomenon could be responsible for the observed performance improvement at higher growth temperatures. Nevertheless, it is also worth noticing that a too high lattice fluorine concentration might negatively influence the system reactivity promoting recombination losses of photogenerated e^-/h^+.[17] Hence, the actual hydrogen production rates result from a delicate balance of various effects, and the identification of the optimal doping level directly requires the independent control of lattice *vs*. contaminating fluorine content, a challenging issue deserving further investigation.

4. CONCLUSIONS

In conclusion, this work has presented the first example of F-doped Fe_2O_3 nanosystems synthesized by PE-CVD. The target materials have been deposited on Si(100) substrates from Ar-O_2 plasmas using a Fe(II) diketonate-diamine molecular compound as single-source precursor for both iron and fluorine. Irrespective of the adopted growth temperature (300–500 °C), F:α-Fe_2O_3 systems free from other iron oxide polymorphs were obtained. The surface copresence of lattice fluorine and contaminating CF_x species, whose overall amount underwent a systematic decrease at higher growth temperatures, was observed. Interestingly, in-depth compositional analyses revealed that, while the latter was limited to the sample surface, the former was homogeneously distributed into the iron oxide matrix. The F:α-Fe_2O_3 materials were tested as catalysts in the photoreforming of water/ethanol solutions under simulated sunlight irradiation, resulting in hydrogen yields among the best ever reported in the literature for supported oxide-based systems. The remarkable H_2 evolution, along with the appreciable time stability, highlight the proposed strategy as an effective mean to fabricate highly efficient photocatalysts and evidences the potential of fluorine doping to obtain improved system performances. As a perspective for the development of this work, future efforts will be devoted to achieve an independent control of lattice versus contaminating fluorine by a proper choice of the processing conditions.

Acknowledgments: The research leading to these results has received funding from the European Community's Seventh Framework Program (FP7/2007-2013; grant agreement no. ENHANCE-238409), as well as by Padova University ex-60% 2012 (no. 60A03-5517), PRAT 2010 (no. CPDA102579) and Regione Lombardia-INSTM "ATLANTE" projects. Tiziano Montini, Valentina Gombac and Paolo Fornasiero acknowledge financial support from Trieste University (FRA 2011 project), INSTM, Fondazione CRTrieste and Fondazione Benefica Kathleen Foreman Casali. The authors are also grateful to Mr. A. Ravazzolo (CNR-ISTM, Padova, Italy) for technical and synthetic assistance.

References and Notes

1. V. R. Satsangi, S. Kumari, A. P. Singh, R. Shrivastav, and S. Dass, *Int. J. Hydrogen Energy* 33, 312 (**2008**).
2. A. Gasparotto, D. Barreca, D. Bekermann, A. Devi, R. A. Fischer, P. Fornasiero, V. Gombac, O. I. Lebedev, C. Maccato, T. Montini, G. Van Tendeloo, and E. Tondello, *J. Am. Chem. Soc.* 133, 19362 (**2011**).
3. M. Cornuz, M. Grätzel, and K. Sivula, *Chem. Vapor Deposition* 16, 291 (**2010**).
4. E. Thimsen, F. Le Formal, M. Grätzel, and S. C. Warren, *Nano Lett.* 11, 35 (**2010**).
5. B. Klahr, S. Gimenez, F. Fabregat-Santiago, T. Hamann, and J. Bisquert, *J. Am. Chem. Soc.* 134, 4294 (**2012**).
6. G. K. Pradhan, S. Martha, and K. M. Parida, *ACS Appl. Mater. Interfaces* 4, 707 (**2011**).
7. D. Barreca, G. Carraro, V. Gombac, A. Gasparotto, C. Maccato, P. Fornasiero, and E. Tondello, *Adv. Funct. Mater.* 21, 2611 (**2011**).
8. X. Chen, S. Shen, L. Guo, and S. S. Mao, *Chem. Rev.* 110, 6503 (**2010**).
9. S. Liu, J. Yu, B. Cheng, and M. Jaroniec, *Adv. Colloid Interface Sci.* 173, 35 (**2012**).
10. D. A. Wheeler, G. Wang, Y. Ling, Y. Li, and J. Z. Zhang, *Energy Environ. Sci.* 5, 6682 (**2012**).
11. A. M. Jubb and H. C. Allen, *ACS Appl. Mater. Interfaces* 2, 2804 (**2010**).
12. S. Mathur, M. Veith, V. Sivakov, H. Shen, V. Huch, U. Hartmann, and H. B. Gao, *Chem. Vapor Deposition* 8, 277 (**2002**).
13. K. Sivula, F. Le Formal, and M. Grätzel, *ChemSusChem* 4, 432 (**2011**).
14. W. D. Chemelewski, N. T. Hahn, and C. B. Mullins, *J. Phys. Chem. C* 116, 5255 (**2012**).
15. G. Wang, Y. Ling, D. A. Wheeler, K. E. N. George, K. Horsley, C. Heske, J. Z. Zhang, and Y. Li, *Nano Lett.* 11, 3503 (**2011**).
16. H. Seo, L. R. Baker, A. Hervier, J. Kim, J. L. Whitten, and G. A. Somorjai, *Nano Lett.* 11, 751 (**2010**).
17. B. Liu, M. Gu, X. Liu, S. Huang, and C. Ni, *Appl. Phys. Lett.* 97, 122101 (**2010**).
18. S. Chen, S. Sun, H. Sun, W. Fan, X. Zhao, and X. Sun, *J. Phys. Chem. C* 114, 7680 (**2010**).

19. Y. Zhao, X. Du, X. Wang, J. He, Y. Yu, and H. He, *Sens. Actuators B* 151, 205 **(2010)**.

20. D. Chen, Z. Jiang, J. Geng, J. Zhu, and D. Yang, *J. Nanopart. Res.* 11, 303 **(2009)**.

21. S. Sumitsawan, J. Cho, M. L. Sattler, and R. B. Timmons, *Environ. Sci. Technol.* 45, 6970 **(2011)**.

22. J. Xu, Y. Ao, D. Fu, and C. Yuan, *Appl. Surf. Sci.* 254, 3033 **(2008)**.

23. D. Barreca, G. Carraro, A. Gasparotto, C. Maccato, R. Seraglia, and G. Tabacchi, *Inorg. Chim. Acta* 380, 161 **(2012)**.

24. D. Barreca, G. Carraro, A. Devi, E. Fois, A. Gasparotto, R. Seraglia, C. Maccato, C. Sada, G. Tabacchi, E. Tondello, A. Venzo, and M. Winter, *Dalton Trans.* 41, 149 **(2012)**.

25. J. Zheng, R. Yang, L. Xie, J. Qu, Y. Liu, and X. Li, *Adv. Mater.* 22, 1451 **(2010)**.

26. M. Cargnello, A. Gasparotto, V. Gombac, T. Montini, D. Barreca, and P. Fornasiero, *Eur. J. Inorg. Chem.* 2011, 4309 **(2011)**.

27. D. Barreca, A. Gasparotto, E. Tondello, C. Sada, S. Polizzi, and A. Benedetti, *Chem. Vap. Dep.* 9, 199 **(2003)**.

28. D. Briggs and M. P. Seah, Practical Surface Analysis: Auger and X-ray Photoelectron Spectroscopy, 2nd edn., John Wiley and Sons, New York **(1990)**.

29. N. Strataki, V. Bekiari, D. I. Kondarides, and P. Lianos, *Appl. Catal., B* 77, 184 **(2007)**.

30. S. Y. Reece, J. A. Hamel, K. Sung, T. D. Jarvi, A. J. Esswein, J. J. H. Pijpers, and D. G. Nocera, *Science* 334, 645 **(2011)**.

31. Pattern # 33-0664, JCPDS **(2000)**.

32. W. M. Haynes, Handbook of Chemistry and Physics, 92nd edn., CRC Press, Boca Raton, FL **(2011–2012)**.

33. I. V. Chernyshova, M. F. Hochella, Jr, and A. S. Madden, *Phys. Chem. Chem. Phys.* 9, 1736 **(2007)**.

34. B. Zhang, Y. Tian, J. X. Zhang, and W. Cai, *Mater. Lett.* 64, 2707 **(2010)**.

35. J. F. Moulder, W. F. Stickle, P. E. Sobol, and K. D. Bomben, Handbook of of X-ray Photoelectron Spectroscopy, Perkin Elmer Corporation, Eden Prairie, MN **(1992)**.

36. D. Barreca, D. Bekermann, E. Comini, A. Devi, R. A. Fischer, A. Gasparotto, M. Gavagnin, C. Maccato, C. Sada, G. Sberveglieri, and E. Tondello, *Sens. Actuators B* 160, 79 **(2011)**.

37. W.-L. Lu, T.-W. Kuo, C.-H. Huang, N.-F. Wang, Y.-Z. Tsai, M. W. Wang, C.-I. Hung, and M.-P. Houng, *Thin Solid Films* 520, 35 **(2011)**.

38. D. Li, H. Haneda, N. K. Labhsetwar, S. Hishita, and N. Ohashi, *Chem. Phys. Lett.* 401, 579 **(2005)**.

Received: 5 August 2012. Accepted: 12 October 2012.